ADVANCED FUNCTIONAL MATERIALS
www.afm-journal.de

Radial X-Ray Diffraction Study of Superhard Early Transition Metal Dodecaborides under High Pressure

Jialin Lei, Georgiy Akopov, Michael T. Yeung, Jinyuan Yan, Richard B. Kaner, and Sarah H. Tolbert**

The deformation behavior of the three metal dodecaborides (YB_{12}, ZrB_{12}, and $Zr_{0.5}Y_{0.5}B_{12}$) is investigated using radial X-ray diffraction under non-hydrostatic compression up to ≈60 GPa with a goal of understanding how bonding and metal composition control hardness. $Zr_{0.5}Y_{0.5}B_{12}$, which has the highest Vickers hardness (Hv = 45.8 ± 1.3 GPa at 0.49 N load), also shows the highest bulk modulus (K_0 = 320 ± 5 GPa). The 0.49 N hardness for ZrB_{12} and YB_{12} are both lower and very similar, and both show lower bulk moduli (K_0 = 276 ± 7 GPa, and K_0 = 238 ± 6 GPa, respectively). Differential stress is then measured to study the strength and strength anisotropy. $Zr_{0.5}Y_{0.5}B_{12}$ supports the highest differential stress, in agreement with its high hardness, a fact that likely arises from atomic size mismatch between Zr and Y combined with the rigid network of boron cages. The (200) plane for all samples supports the largest differential strain, while the (111) plane supports the smallest, consistent with the theoretically predicted slip system of {111} [$\bar{1}\bar{1}2$]. Strain softening is also observed for ZrB_{12}. Finally, the full elastic stiffness tensors for ZrB_{12} and YB_{12} are solved. ZrB_{12} is the most isotropic, but the extent of elastic anisotropy for all dodecaborides studied is relatively low due to the highly symmetric boron cage network.

1. Introduction

With the rapid development of modern structural materials grows a pressing need for new tools that shape and form them. Modern forming requires long-lasting cutting, grinding, and polishing tools, materials with high hardness, and excellent toughness. Superhard materials, with their Vickers hardness greater than 40 GPa, meet these stringent requirements.[1] Diamond, as one of the most well-known superhard materials, possesses an extreme hardness of 70–110 GPa[2] in its single crystal form and a bulk modulus (K) of 442 GPa;[3] however, it is not suitable for machining ferrous metals due to the formation of brittle carbides which shortens its lifetime.[4,5] Moreover, because of its poor oxidative stability, diamond cannot be used in air at high temperatures.[6]

Despite these drawbacks, exploration into the origin of superhardness in diamond still provides valuable insights into what makes diamond superhard, and guides the development of new superhard materials. It is believed that the high shear modulus of diamond stems from the 3D network of strong, short carbon–carbon covalent bonds, while its high bulk modulus arises from its high valence electron density (0.705 electrons Å^{-3}); together, these make diamond superhard. Tungsten tetraboride (WB_4) exemplifies these design rules, with a high Vickers hardness (Hv = 43.3 ± 2.9 GPa under a load of 0.49 N),[7,8] relatively easy synthesis at ambient pressure, as well as low cost and good incompressibility (K = 324 ± 3 GPa).[9] The high valence electron density in tungsten mirrors the ultra-incompressibility of diamond, and this, combined with a network of rigid boron cages,[10] mimics the bonding motif in diamond, which transforms the originally soft elemental W (Hv = 3.4–4.6 GPa)[11] into superhard WB_4.[12,13] As can be seen in **Figure 1**a, WB_4 consists of alternating hexagonal layers of boron and tungsten with partially occupied sites. The boron atoms sitting in the unoccupied W sites and those in the hexagonal layers form distorted cuboctahedral cages.[14] These rigid boron cages bind the boron sheets together and thus help pin dislocation motion along the primary basal slip system in the hexagonal lattice. Because of this 3D boron network, WB_4 also shows less strength anisotropy, confirming the positive influence of cage structures in developing next generation superhard materials.[15] Moreover, dodecaboride forming metals (Zr, Y, Er, Tb, Ho, and Dy) can be added to WB_4,

Dr. J. Lei, Dr. G. Akopov,[+] Dr. M. T. Yeung,[++] Prof. R. B. Kaner, Prof. S. H. Tolbert
Department of Chemistry and Biochemistry
University of California, Los Angeles (UCLA)
Los Angeles, CA 90095, USA
E-mail: kaner@chem.ucla.edu; tolbert@chem.ucla.edu
Dr. J. Yan
Advanced Light Source
Lawrence Berkeley National Lab
Berkeley, CA 94720 USA
Prof. R. B. Kaner, Prof. S. H. Tolbert
Department of Materials Science and Engineering
University of California, Los Angeles (UCLA)
Los Angeles, CA 90095 USA
Prof. R. B. Kaner, Prof. S. H. Tolbert
California Nano Systems Institute (CNSI)
University of California, Los Angeles (UCLA)
Los Angeles, CA 90095 USA
The ORCID identification number(s) for the author(s) of this article can be found under https://doi.org/10.1002/adfm.201900293.
[+]Present address: Department of Chemistry, Iowa State University, Ames, IA 50011, USA and Ames Laboratory, U.S. Department of Energy, Ames, IA 50011, USA
[++]Present address: Department of Chemistry, Northwestern University, Evanston, IL 60208, USA

DOI: 10.1002/adfm.201900293

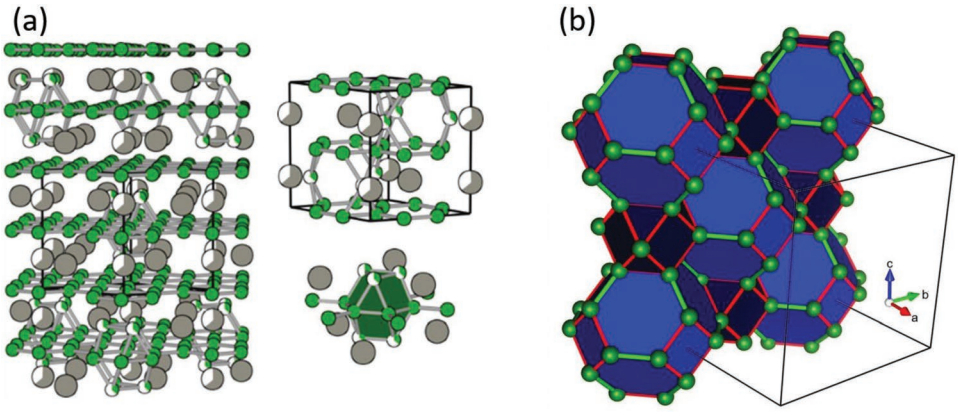

Figure 1. A polyhedral view of crystal structures of a) WB_4 and b) metal dodecaborides. Part (a) was reproduced with permission.[10] Copyright 2015, National Academy of Sciences.

generating remarkable surface morphologies, which enhance the extrinsic hardness of this tetraboride.[16]

This finding inspired us to turn our attention to the metal dodecaborides (MB_{12}) such as YB_{12}, ZrB_{12}, and their solid solutions, which have the ultimate cage structure as shown in Figure 1b. In MB_{12}, the metal atoms occupy octahedral sites of this cubic structure at the corners and face centers forming an FCC lattice ($Fm\bar{3}m$). Each metal atom is located at the center of a cuboctahedral cluster (blue in color) formed by 24 borons. Smaller clusters (black), formed by 12 borons, can be found at the edge centers and body centers.[17,18] Note that the occurrence of cuboctahedral clusters in WB_4 is at most one for every four metal atoms, whereas it is one per metal atom in MB_{12} structures. Moreover, both the slightly longer red boron–boron bond distances and the shorter green bond distances in Figure 1b for MB_{12} are shorter than those in WB_4 and ReB_2,[19–21] suggesting the potential for high hardness in MB_{12}. Indeed, Akopov et al.[22–24] have recently synthesized ZrB_{12}, YB_{12}, and $Zr_{1-x}Y_xB_{12}$ solid solutions at ambient pressure by arc-melting. The micro-indention hardness tests show that all these dodecaborides are superhard, as expected, with the highest Vickers hardness of 45.8 ± 1.3 GPa at an applied load of 0.49 N achieved by $Zr_{0.5}Y_{0.5}B_{12}$. The hardness for $Y_xZr_{1-x}B_{12}$ solid solutions at different loads can be found in Figure S1 in the Supporting Information. In addition, Ma et al.[25] found that ZrB_{12} is not only superhard, but also highly electrically conductive with a resistivity of only 18 μΩ·cm at room temperature resulting from the network of boron clusters. Their hardness tests on ZrB_{12} single crystals suggests that, like diamond, it is mechanically isotropic in the {100}, {110}, and {111} planes.

Interestingly, all metal dodecaborides stable at ambient pressure have stringent requirements on the metal atom radii, with zirconium (r_{at} = 1.55 Å, $r_{CN\,=\,12}$ = 1.603 Å) forming the dodecaboride with the smallest lattice parameter, and yttrium (r_{at} = 1.80 Å, $r_{CN\,=\,12}$ = 1.801 Å) the largest.[26,27] As a result, the unit cell volumes for ZrB_{12} (405.5 Å^3) and YB_{12} (422.7 Å^3) are the lower and upper bounds necessary to meet the size requirement for stable dodecaborides, respectively. The Vickers hardness and bulk modulus for ZrB_{12} have been measured,[24] but only under hydrostatic conditions,[28] and nonhydrostatic conditions more closely resembling those under an indenter's tip in a micro-indentation hardness test[29] have not yet been examined. For YB_{12}, the volume compression behavior at high pressure has yet to be studied in any form. Additionally, although there are some theoretical calculations about the elastic stiffness constants for transition metal dodecaborides,[24,30,31] direct experimental measurements have hitherto not been performed. Finally, and perhaps most importantly, the mechanisms for the hardness enhancement in $Zr_{0.5}Y_{0.5}B_{12}$ and the solid-solution-induced change in compressibility are also not clear.

Here, we have performed radial X-ray diffraction (RXRD)[32–34] experiments under nonhydrostatic compression on ZrB_{12}, YB_{12}, and $Zr_{0.5}Y_{0.5}B_{12}$ with the goal of determining their bulk moduli and examining differential stress for each sample in a lattice plane–specific manner up to ≈60 GPa. Note that the plateau value of the differential stress has been considered as a good estimate of yield strength for many materials,[35–42] which in turn is strongly related to the hardness. The lattice-specific differential stress, which can only be measured from radial diffraction rather than the traditional axial diffraction, can thus provide significant insights into materials hardness. The nonhydrostatic stress also needs to be taken into account even for axial diffraction when determining bulk modulus, because a completely hydrostatic environment cannot be maintained above 15 GPa due to the freezing of all pressure-transmitting medium at room temperature.[43–45] Diffraction in a radial geometry thus provides insight into both the elastic and plastic behavior of these materials.

2. Results and Discussion

ZrB_{12}, YB_{12}, and $Zr_{0.5}Y_{0.5}B_{12}$ were individually compressed under nonhydrostatic conditions in the diamond anvil cell (DAC) up to ≈60 GPa. Radial diffraction patterns were recorded at steps of ≈4 GPa, and the pressure was derived from the equation of state (EOS) of Au,[46] using its measured unit cell volume at φ = 54.7°, which produces lattice deformations equivalent to those obtained under hydrostatic conditions. Representative XRD patterns are shown in **Figure 2**, and the experimental data are indexed and compared to the stick reference patterns from the Joint Committee on Powder Diffraction Standards and by Akopov et al.[22] Each sample maintains their cubic structure up to the highest

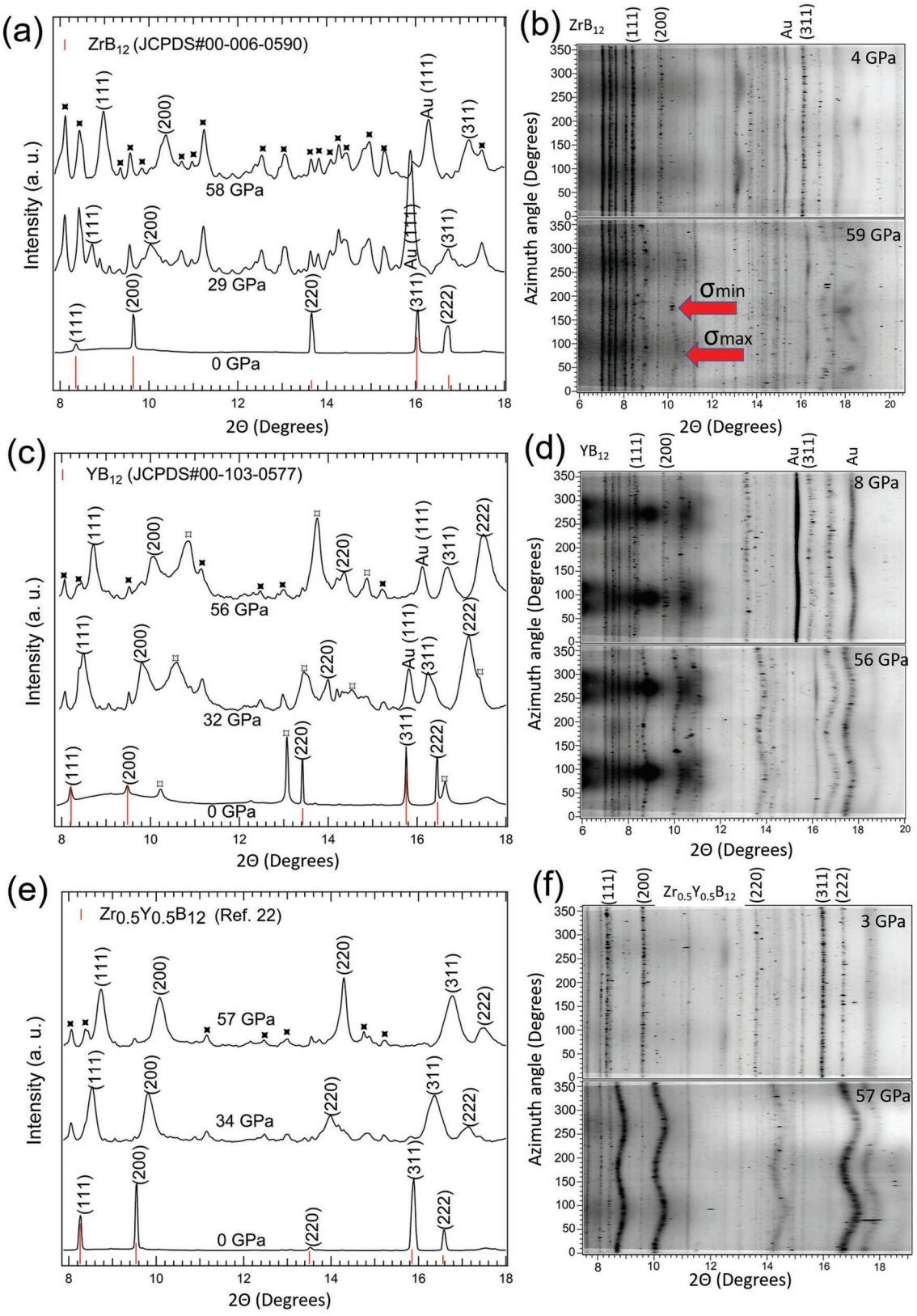

Figure 2. Representative synchrotron 1D XRD patterns and 2D azimuthally unrolled patterns with increasing pressure for a,b) ZrB_{12}, c,d) YB_{12}, and e,f) $Zr_{0.5}Y_{0.5}B_{12}$. Au was used for the in situ pressure calibration. Peaks marked with solid symbols at high pressure stem from the boron gasket. Peaks marked with open symbols in (b) correspond to a YB_{66} impurity.

pressure in our experiments, and a clear shift toward higher angles can be observed with increasing pressure, indicating a decrease in unit cell volume with increasing compression.

In addition to the dodecaboride phase, the peaks labeled with solid star symbols stem from diffraction from the boron gaskets, as indicated by the fact that they do not shift with pressure. This can be confirmed from the azimuthally (0°–360°) unrolled cake patterns where the diffraction lines for the dodecaboride phase become curved at high pressure due to the nonhydrostatic compression. Here the high stress direction and low stress directions are labeled with red arrows. Any diffraction peaks that remain straight during the compression are not under pressure. The ambient pressure patterns were not collected in the DAC, and therefore they do not contain diffraction signals from the boron gasket, which is generally unavoidable for high-pressure radial diffraction data. Fortunately, the diffraction from the boron gasket does not affect the measurements, because these high-pressure experiments are conducted in a lattice-specific manner. Since the diffraction from the boron gasket does not overlap with the phase of interest and they do not shift with the pressure as shown in Figure 2, they can be clearly identified and introduce no ambiguity to the results. Moreover, the fact that the diffraction lines for the boron gasket are all straight, rather than curved, indicates that the majority of the gasket is not under pressure, and that the specimen is indeed the load-bearing material.

In addition to the boron gasket, we found that the YB_{12} sample contains an impurity phase of YB_{66} that is labeled with an open star symbol and is present across the studied pressure range in Figure 2c. YB_{66} possesses a giant cubic unit cell containing 1584 boron atoms and 24 Y atoms.[22] Since it has no overlapping diffraction peaks with the phase of interest, the impurity phase can be recognized unambiguously and the data analysis for YB_{12} is not affected. Given that the diffraction lines (111), (200), and (311) have the highest intensity among the observed patterns and can be detected at all pressures, we chose these three peaks to define the volume deformation behavior and strength anisotropy for each sample.

The pressure dependence of the *d*-spacings and lattice constants for ZrB_{12}, YB_{12}, and $Zr_{0.5}Y_{0.5}B_{12}$ are summarized in **Figure 3** and Table S1 in the Supporting Information. Note that all the *d*-spacings were measured at the hydrostatic equivalent direction and that the data collected under decompression are labeled with open symbols. The errors for the pressure at each compression step are shown in Table S1 in the Supporting Information and the values are typical of those obtained in other radial diffraction experiments. The difference in atomic size between Zr and Y is relatively small (<15%), but as shown in Figure 3, because data are collected across a range of pressure, different trends across the three materials can be easily distinguished. As can be seen in the figure, the *d*-spacings show a continuous linear decrease as a function of pressure without any abrupt variations, suggesting that the samples are able to maintain the cubic structure upon compression and decompression up to ≈60 GPa.

Vegard's law states that the lattice constant of a solid solution should be a weighted average of the lattice constants of its two constituents.[47] The lattice constant for $Zr_{0.5}Y_{0.5}B_{12}$ measured at ambient pressure (7.454 Å) is in good agreement with the predicted value calculated using Vegard's law (7.453 Å), indicating that ZrB_{12} and YB_{12} form a nearly ideal solid solution. For a

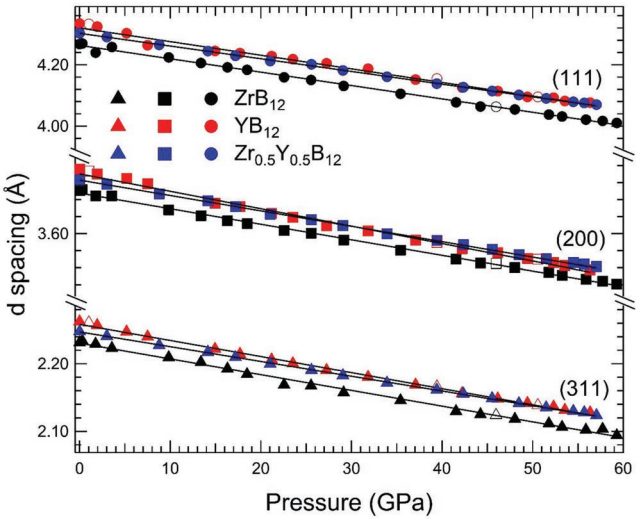

Figure 3. Measured *d*-spacings for the (111), (200), and (311) lattice planes as a function of pressure. Error bars that are smaller than the size of the symbols have been omitted.

series of lower pressures shown in Figure 3, the *d*-spacings for $Zr_{0.5}Y_{0.5}B_{12}$ continue to lie essentially halfway between ZrB_{12} and YB_{12}, suggesting it also follows Vegard's law at modest pressure. This is attributed to the fact that all materials have the same cubic-UB_{12} ($Fm\bar{3}m$) structure, similar electronegativities for the metals, and relatively small differences in their radii (<15%). As the pressure increases, however, the *d*-spacings for $Zr_{0.5}Y_{0.5}B_{12}$ begin to deviate from the average value of ZrB_{12} and YB_{12} and approach the YB_{12} boundary, indicating deviation from Vegard's law at higher pressure. Interestingly, the *d*-spacings of the (200) lattice plane for $Zr_{0.5}Y_{0.5}B_{12}$ crosses YB_{12} at ≈35 GPa, indicating significantly decreased compressibility for the $Zr_{0.5}Y_{0.5}B_{12}$ solid solution.

One possible explanation for this behavior is that the lattice constant for $Zr_{0.5}Y_{0.5}B_{12}$ is fundamentally too small for the Y atoms even though it follows Vegard's law at ambient pressure. As mentioned above, Zr and Y represent the lower and upper bounds in size for metals that can coordinate with 12 boron atoms. The fact that the *d*-spacings for $Zr_{0.5}Y_{0.5}B_{12}$ are closer to the YB_{12} values implies that repulsion between the larger Y atom and the boron cage limits the compressibility of this system at higher pressures. In other words, the unit cell for the $Zr_{0.5}Y_{0.5}B_{12}$ can be thought of as being partly precompressed at ambient pressure to accommodate the conflicting energetic need to avoid repulsion between Y and the boron cage and to optimize bonding between Zr and the boron cage. Because of the rigid structure of the material, which cannot distort to simultaneously satisfy both demands, and because of the increasing energetic dominance of the repulsive interactions at high pressure, the observed lattice evolution occurs. The corollary is that the solid solution may have greater capability to resist further compression.

The pressure-dependent peak position was then used to calculate the fractional unit cell volume for each sample as a function of pressure in the range from 0 to ≈60 GPa, as shown in **Figure 4**. The compression data were fit to the third-order Birch–Murnaghan EOS yielding a bulk modulus of 276 ± 7 GPa ($K_0' = 2.0 \pm 0.4$), 238 ± 6 GPa ($K_0' = 3.0 \pm 0.1$), and 320 ± 5 GPa

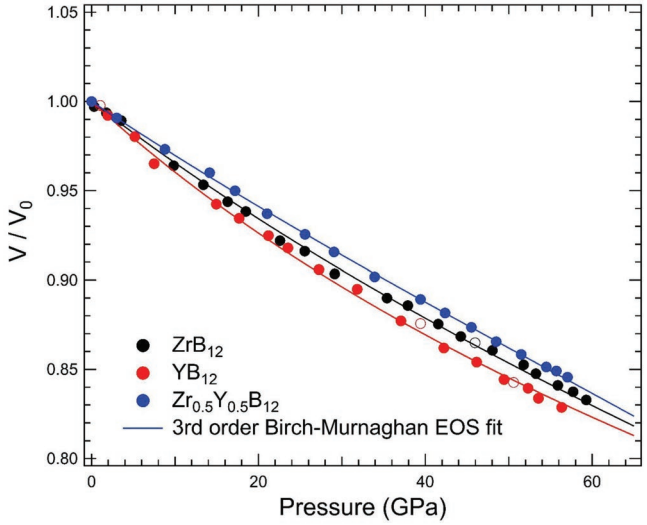

Figure 4. Hydrostatic compression curves for ZrB_{12} (black), YB_{12} (red), and $Zr_{0.5}Y_{0.5}B_{12}$ (blue) obtained from radial diffraction data at $\varphi = 54.7°$. The solid lines are the best fits to the third-order Birch–Murnaghan EOS.

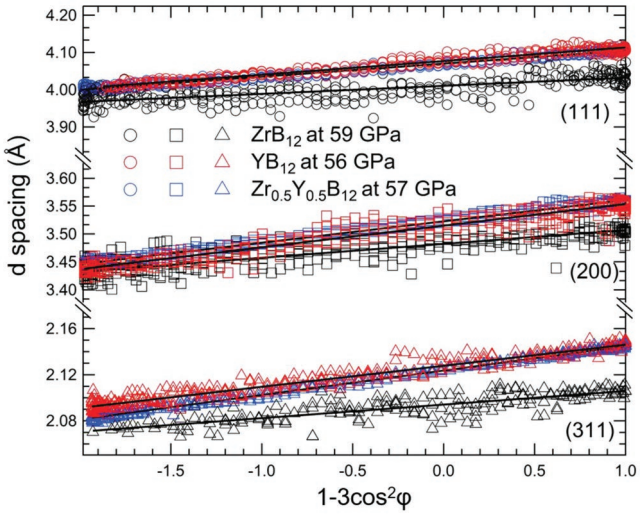

Figure 5. Dependence of observed *d*-spacings on $(1 - 3\cos^2\varphi)$. The solid lines are the best linear fit to the data.

($K_0' = 1.2 \pm 0.1$) for ZrB_{12}, YB_{12}, and $Zr_{0.5}Y_{0.5}B_{12}$, respectively. The EOS in terms of normalized pressure and Eularian strain[48] including the second-order fitting results can be found in Figure S2 in the Supporting Information. $Zr_{0.5}Y_{0.5}B_{12}$, which is the hardest of the three compounds, also possesses the highest incompressibility among the three samples, for the reasons discussed above. It therefore supports our assumption that incompressibility is a design parameter for high hardness. The trends in the other materials can also be rationalized: bulk modulus is directly related to the valence electron density.[4,49] Zirconium has one electron more than yttrium and is also smaller than yttrium in atomic size, suggesting that the valence electron density for ZrB_{12} is higher than for YB_{12}. This is in good agreement with the trends in bulk modulus.

To improve confidence in the use of nonhydrostatic data to determine the bulk modulus, we also make comparisons to previously reported values for ZrB_{12}. Due to the lack of a previously reported third-order value for bulk modulus, here we compare only the second-order value. Our measured value for ZrB_{12} ($K_0 = 245 \pm 5$ GPa obtained from second-order fitting with fixed $K_0' = 4$) is consistent with the theoretical value of 243.5 GPa[30] and previous experimental values of 234–249 GPa[50,51] within the uncertainty. It is, however, slightly higher than the value of 221 ± 8 GPa reported by Ma et al.[25] The difference may arise from the intrinsic difficulty in performing high-pressure X-ray diffraction on compounds that have low metal contents such as dodecaborides.

Bulk modulus is a measure of elastic deformation reflecting the resistance to the volume change with respect to pressure. It is not, however, directly related to the hardness which is the resistance to plastic deformation. There are many factors that contribute to hardness such as the strength and directionality of interatomic bonds, defect density, micro- or nanostructuring, and grain size. The yield strength is believed to be one of the most significant determining factors for hardness. By running radial diffraction, we are also able to measure the ratio of yield strength to the shear modulus (t/G), known as differential strain, in a lattice-specific manner, in addition to measuring bulk modulus.

Figure 5 shows the dependence of the *d*-spacings as a function of $(1 - 3\cos^2\varphi)$ for the selected planes at the highest pressure, which presents the expected linear variation according to Equation (2). $Q(hkl)$ can be extracted from the slope of each line and it is directly related to t/G, as indicated in Equation (3). Values of t/G for selected planes are plotted as a function of pressure for ZrB_{12} (black), YB_{12} (red), and $Zr_{0.5}Y_{0.5}B_{12}$ (blue) in **Figure 6**. The $t(111)/G$, $t(200)/G$, and $t(311)/G$ for the three samples show similar behavior at the beginning of compression. They all increase almost linearly when the pressure is lower than ≈40 GPa indicating the samples are still within the elastic regime. Upon further compression, the rate slows and eventually plateaus for YB_{12} and $Zr_{0.5}Y_{0.5}B_{12}$, which indicates the beginning of plastic deformation. This is the point where t has reached its limiting value and should correspond to the yield strength. Note that because yielding behavior occurs across a range of pressure in the plateau region of the differential strain/stress curve, this value is an ideal way to compare samples, because it is not affected by the pressure step size or details of sample loading. Interestingly, the t/G ratios for ZrB_{12} also exhibit a plateau at a pressure of 40–50 GPa. This plateau is then followed by a decrease at pressures higher than ≈50 GPa, indicating a strain softening phenomenon. This may due to the grain boundary sliding or grain rotation at such high pressures.[52–56] Alternatively, the stress may be released through a new slip system enabled by pressure-induced bond rearrangement, a phenomenon previously observed by our group for WB_4.[9] Additional investigations using simulations or texture analysis would be needed to verify the dominant mechanisms for plastic deformation at high pressure. Given that the (111) plane for the three samples always supports the lowest t/G ratio, it is very likely to be a slip plane, which is consistent with the slip system of {111} $[\bar{1}\bar{1}2]$ reported for ZrB_{12}.[25]

We note that materials with high differential strain (t/G) are not necessarily hard, since a very low shear modulus like

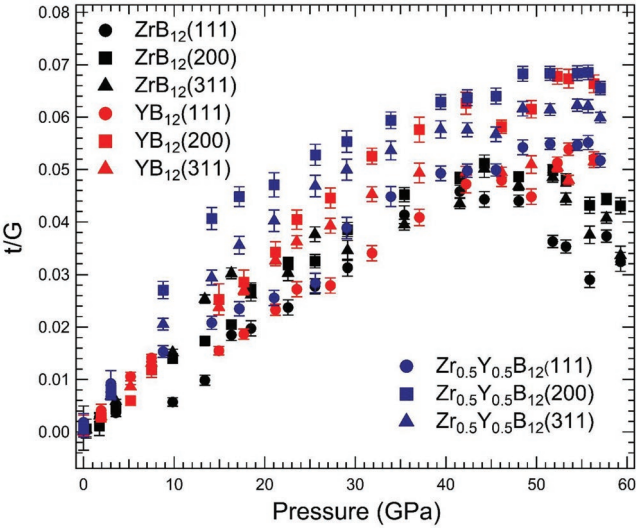

Figure 6. Ratio of differential stress t to aggregate shear modulus G as a function of pressure for three different lattice planes of the three dodecaborides studied in this work. Keys on the figure indicates material and lattice plane.

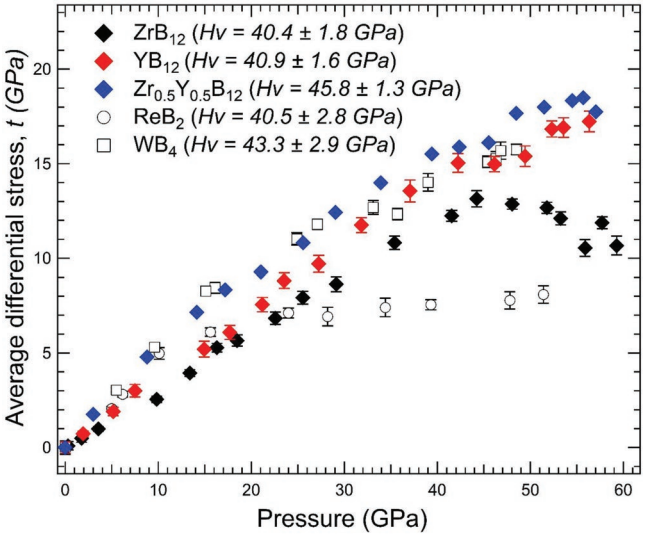

Figure 7. Evolution of the average differential stress for the three dodecaborides studied here, along with selected other representative superhard materials,[12] all as a function of pressure. A strong correlation between hardness (indicated in the key) and average value of t is observed.

that found in a soft elastic material can also produce a high strain. Because of this, it is important to calculate t in addition to t/G, something that is often hampered by a lack of measured values of G. Here, we use the theoretical shear modulus of 204 GPa for ZrB_{12} and 220 GPa for YB_{12}.[30] Since neither a computational nor experimental shear modulus for $Zr_{0.5}Y_{0.5}B_{12}$ has been reported, we used the average of the values for the two end members as an approximation. We acknowledge that this choice of a shear modulus is not ideal because the shear modulus is influenced by variations in composition for solid solutions. For hard materials and especially for transition metal borides, however, the shear modulus does not generally change very much across a family of compounds, and so the average value has been shown to be a reasonable approximation of the solid-solution value.[57] The shear moduli at elevated pressures were approximated by extrapolating the zero-pressure values using the pressure derivative dG/dP of 1.5, which is typical for ceramics,[58] and is also used for transition metal borides such as WB,[59] WB_4,[15] and boron-rich superhard materials such as B_6O.[40]

To look at trends in the differential stress, we looked at the average value of t for each material, as shown in **Figure 7**. Because the trends in each lattice plane are so similar up to 50 GPa, we use an average value obtained by taking the average of the $t(111)$, $t(200)$, and $t(311)$ values, and compared these curves with ReB_2 and WB_4 in Figure 7. A remarkably good correlation between the trends in hardness and the trends in the plateau values of the differential stress can be found across all five samples. As can be seen in the figure, $Zr_{0.5}Y_{0.5}B_{12}$ supports the highest differential stress with a plateau value of 17.5 GPa followed by YB_{12} and ZrB_{12}. This is indeed consistent with our hardness test where the solid solution shows the highest hardness. Both the hardness and plateau stress of WB_4 approach that of $Zr_{0.5}Y_{0.5}B_{12}$, while ReB_2 is more similar to ZrB_{12} in both hardness and plateau stress. Note that the hardness values for ZrB_{12} and YB_{12} are very close, while YB_{12} supports a higher differential stress. This is potentially because the indentation hardness is affected by both intrinsic (i.e., strength and directionality of bonding, composition, and crystal structure) and extrinsic factors (i.e., grain size and nanotwinned structures).[60] In radial diffraction, we measured the deformation behavior for the lattice, which only reflects the intrinsic strength of the material;[61,62] allowing us to distinguish these two factors. The fact that ZrB_{12} supports a lower differential stress than YB_{12} could suggest that some extrinsic hardening effects may be active in ZrB_{12}.

Knowing t and K, we can then determine the elastic stiffness constants using Equations (8)–(10). These calculations are performed only for the two end members because of the lack of an accurate shear modulus for the solid solution which may induce errors in the value of t. The dependence of $Q(hkl)$ on $3\,\Gamma(hkl)$ at representative pressures is plotted in Figure S3 in the Supporting Information and shows the expected linear variation. The pressure-dependent elastic constants for ZrB_{12} and YB_{12} are shown in **Figure 8**. Note that the moduli at low pressures are not plotted because the error in t is higher at low pressure, and so these low-pressure values are unreliable. The solid line in the figure is the best fit to the third-order finite strain equation yielding the ambient values of elastic moduli. The plot of normalized elastic constants varying with Eularian strain can be found in Figure S4 in the Supporting Information. The larger value of c_{11} for ZrB_{12} suggests that it has a higher linear incompressibility along the ⟨100⟩ direction. For cubic symmetry, the bulk modulus strongly depends on c_{11} and c_{12}, with higher values of c_{11} and c_{12} resulting in a higher bulk modulus. The high values of c_{44} for YB_{12} reflect greater capability to prevent shearing along [100], implying better yield strength, which is consistent with our differential stress data.

Given these $[c_{ij}]$ values, we can then examine the Zener ratio, $2c_{44}/(c_{11}-c_{12})$, to see if these materials are elastically

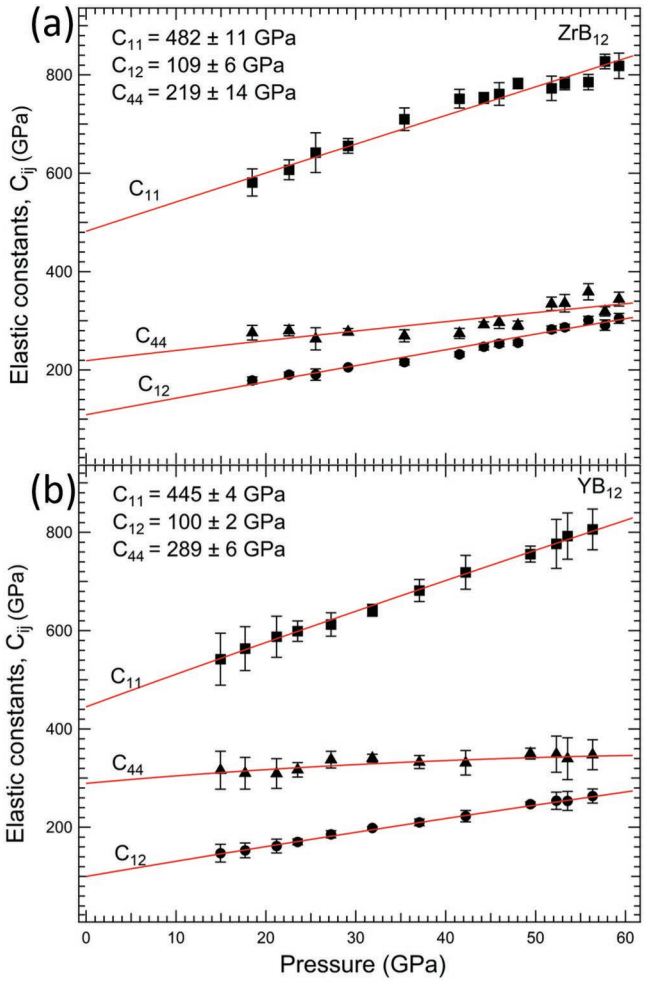

Figure 8. Elastic moduli for ZrB_{12} and YB_{12} as a function of pressure.

isotropic. The Zener factors for ZrB_{12} and YB_{12} are 1.2 and 1.7, respectively, suggesting that neither of them is isotropic, but the extent of anisotropy is quite weak, especially for ZrB_{12} since its ratio is closer to unity. Most diborides such as OsB_2 and ReB_2 consist of alternating metal and boron layers, which lacks the constrained bonding between layers leading to much higher anisotropy. The 3D covalent network of boron cages in the dodecaborides should be more structurally isotropic. Like diamond, dodecaborides belong to the isotropic face-centered cubic Bravais Lattice. Their anisotropic nature can also be observed qualitatively in Figure 6, where the difference in t/G for the three planes for ZrB_{12} is smaller compared to the other two samples.

Finally, the differential stress under the Reuss condition for ZrB_{12} and YB_{12} was calculated using the elastic stiffness constants according to Equation (5) and is plotted in **Figure 9**. We note that the values under the Voigt condition are not included because the elastic moduli were obtained using the assumption of Reuss conditions. As can be seen in the figure, the trends are very similar to those shown in Figure 6, with the (200) plane for YB_{12} supporting the highest differential stress with a plateau value of 16–18 GPa, while the (111) plane shows the lowest t value. A similar trend in $t(hkl)$ can be observed for ZrB_{12}, but

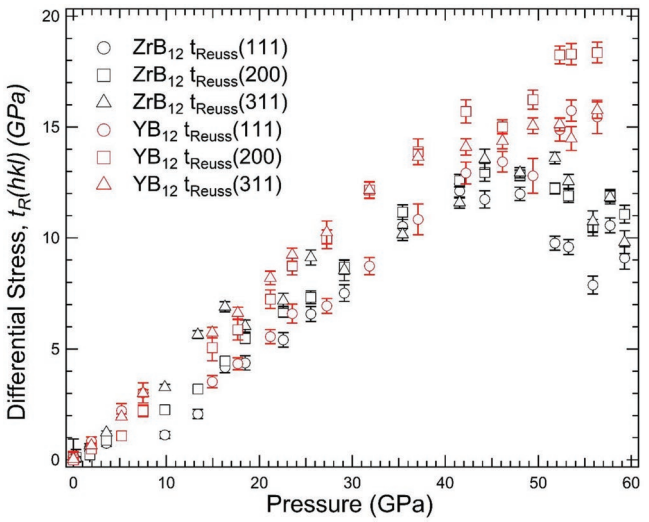

Figure 9. Differential stress as a function of pressure for selected lattice planes in ZrB_{12} and YB_{12} under Reuss (iso-stress) conditions.

note that the yield strength of its strongest plane is still slightly lower than that of the weakest plane for YB_{12} confirming that YB_{12} is intrinsically harder than ZrB_{12}.

3. Conclusions

ZrB_{12}, YB_{12}, and $Zr_{0.5}Y_{0.5}B_{12}$ were studied and compared using synchrotron-based XRD under nonhydrostatic compression up to ≈60 GPa. The hydrostatic compression curves were obtained at $\varphi = 54.7°$ and used to calculate bulk moduli by fitting to the third-order Birch–Murnaghan EOS. $Zr_{0.5}Y_{0.5}B_{12}$ was found to be the least compressible, followed by ZrB_{12} and YB_{12}. Lattice-dependent strength anisotropy was further investigated. We found that the (200) plane supports the greatest differential stress, while the (111) supports the least and is likely a slip plane. The high differential stress measured for $Zr_{0.5}Y_{0.5}B_{12}$ is in good agreement with its high hardness and likely arises from solid solution hardening stemming from the atomic size mismatch between Zr and Y and the rigidity of the boron cage network. The data further indicate that YB_{12} may be intrinsically harder than ZrB_{12}, especially at high pressure, due to the occurrence of strain softening for ZrB_{12} above ≈50 GPa. Finally, three independent elastic constants, c_{11}, c_{12}, and c_{44}, were determined for YB_{12} and ZrB_{12}, which enables us to deduce the directional yield strength for each plane. Besides high harness and bulk modulus, the extent of elastic anisotropy for these materials was found to be low, making them desirable materials for applications such as hard protective coatings. The study on this family of metal dodecaborides allows us to understand the role of cage structures and provides valuable insights into the design rules for new superhard materials.

4. Experimental Section

ZrB_{12}, YB_{12}, and $Zr_{0.5}Y_{0.5}B_{12}$ were synthesized by arc melting from the elements of zirconium (99.5%, Strem Chemicals, USA), yttrium

(99.9%, Strem Chemicals, USA), and amorphous boron (99+%, Strem Chemicals, USA) powder. The molar ratio of metal to boron was kept at 1:20 in order to suppress the formation of lower borides such as diborides (MB_2) or hexaborides (MB_6). In the synthesis, all components were thoroughly mixed together using an agate mortar and pestle. Subsequently, each mixture was transferred to a stainless steel die and was pressed into pellets using a hydraulic Carver press under ≈10 tons. The pellets were then arc melted, under argon to avoid oxidation, with an ≈100 Amp DC current for 1–2 min. The fused ingots were re-arced multiple times to ensure homogeneity. The resultant ingots were then ground to fine powders using a Plattner-style hardened tool-steel mortar and pestle set (Humboldt Mfg., Model H-17270) followed by screening with a No. 635 mesh (20 µm) sieve (Humboldt Mfg.).

The in situ high-pressure RXRD measurements were performed using a panoramic DAC with a culet size of 300 µm at synchrotron beamline 12.2.2 at the Advanced Light Source (ALS, Lawrence Berkeley National Lab). The boron gasket (≈400 µm in diameter and ≈70 µm in thickness) was made of amorphous boron and epoxy[63] with a laser drilled hole (≈50 µm in diameter) at the center as the sample chamber. Powders were loaded individually into the sample chambers of separate DACs and then a small piece of Au foil (≈20 µm) was placed on the top of the sample as a pressure indicator. No pressure-transmitting medium was used to ensure the existence of nonhydrostatic stress in the DAC. More technical details for the DAC can be found in ref. [64].

In the radial diffraction experimental geometry, the incident monochromatic X-ray beam (20 KeV in energy, 20 × 20 µm in beam size) was oriented perpendicular to the compression direction. The diffracted intensity was recorded using an MAR-345 image plate and the pressure was increased in steps of ≈4 GPa. Calibration of the sample-to-detector distance, beam center, and detector tilt was carried out by using a CeO_2 standard and the program FIT2D.[65] Each diffraction line from the azimuthally unrolled diffraction patterns, with 0° and 180° corresponding to the low stress directions and 90° and 270° the high stress directions as shown in Figure 2, was analyzed in program Igor Pro (WaveMetrics, Inc.) using lattice strain theory[66–68] to study the stress state of samples under nonhydrostatic compression.

In radial diffraction, the differential stress t is the difference between σ_1, the radial stress component, and σ_3, the axial stress component, and it can be considered as the lower bond of the material's yield strength according to Von Mises yield criterion[69]

$$t = \sigma_3 - \sigma_1 \leq 2\tau = \sigma_y \tag{1}$$

where τ is the shear strength and σ_y is the yield strength.

The observed d-spacing, $d_m(hkl)$ is a function of $d_p(hkl)$, the d-spacing under the hydrostatic pressure, and φ, the angle between the diamond cell loading axis and diffraction plane normal,[66–68] as given by

$$d_m(hkl) = d_p(hkl)\left[1 + \left(1 - 3\cos^2\varphi\right)Q(hkl)\right] \tag{2}$$

where $Q(hkl)$ is the orientation-dependent lattice strain,[70] which is given by

$$Q(hkl) = \left(\frac{t}{3}\right)\left\{\alpha\left[2G_R(hkl)\right]^{-1} + (1-\alpha)(2G_V)^{-1}\right\} \tag{3}$$

Here, G_V and $G_R(hkl)$ are the Voigt shear modulus under iso-strain[71] conditions and Reuss shear modulus under iso-stress[72] conditions, respectively. For cubic symmetry, the G_V can be written as a function of elastic stiffness moduli[73]

$$5G_V = c_{11} - c_{12} + 3c_{44} \tag{4}$$

The expression for $G_R(hkl)$ in terms of elastic compliances $[S_{ij}]$, is

$$G_R(hkl) = 0.5\left[S_{11} - S_{12} - 3\Gamma(hkl)(S_{11} - S_{12} - 0.5S_{44})\right]^{-1} \tag{5}$$

where $\Gamma(hkl) = (h^2k^2 + k^{2l2} + l^2h^2)/(h^2 + k^2 + l^2)^2$.[68] As shown in Equation (3), the actual shear modulus of a randomly oriented polycrystalline sample is neither $G_R(hkl)$ nor G_V, but a weighted average of the two with an unknown weight given by α. Approximately, the differential stress can be written as a function of aggregate shear modulus, and average lattice strain over observed diffraction peaks, $\langle Q(hkl)\rangle$, as follows[66]

$$t = 6G\langle Q(hkl)\rangle \tag{6}$$

As indicated in Equation (2), $d_m(hkl)$ shows a linear variation as a function of $(1 - 3\cos^2\varphi)$ with a slope of $d_p(hkl)Q(hkl)$ and an intercept of $d_p(hkl)$ (with $x = 0$ corresponding to $\varphi = 54.7°$). The $Q(hkl)$ resolved from the slope can be used to evaluate and describe contributions from both plastic and elastic deformation,[74,75] while the $d_p(hkl)$ obtained from the zero intercept enables the study of its hydrostatic volume compression behavior. The bulk modulus, K_0, and its pressure derivative, K_0', can thus be determined by fitting the compression curve derived from radial diffraction data at the magic angle ($\varphi = 54.7°$) to the third-order Birch–Murnaghan EOS[76]

$$P = 1.5K_0\left[\left(\frac{V}{V_0}\right)^{-\frac{7}{3}} - \left(\frac{V}{V_0}\right)^{-\frac{5}{3}}\right]\left\{1 - 0.75\left(4 - K_0'\right)\left[\left(\frac{V}{V_0}\right)^{-\frac{2}{3}} - 1\right]\right\} \tag{7}$$

Equations (3) and (5) suggest that a plot of $Q(hkl)$ versus $3\Gamma(hkl)$ should show a straight line with an intercept of m_0 and a slope of m_1, given by

$$m_0 = (t/3)(S_{11} - S_{12}) \tag{8}$$

$$m_1 = -(t/3)(S_{11} - S_{12} - S_{44}/2) \tag{9}$$

if the Reuss condition ($\alpha = 1$) is taken. The third equation needed to calculate all the three independent $[S_{ij}]$ terms for a cubic system is thus obtained from the bulk modulus and is given by

$$K = 1/\left[3(S_{11} + 2S_{12})\right] \tag{10}$$

Supporting Information

Supporting Information is available from the Wiley Online Library or from the author.

Acknowledgements

The authors thank M. Kunz for technical support at the Lawrence Berkeley National Laboratory (LBNL) beamline 12.2.2. The authors also thank Professor H.-R. Wenk for equipment support. This work was funded by the National Science Foundation under Grant DMR-1506860 (S.H.T. and R.B.K.), and the UCLA Graduate Division Dissertation Year Fellowship (G.A.), and the Dr. Myung Ki Hong Endowed Chair in Materials Innovation at UCLA (R.B.K.). Radial diffraction experiments were performed at the Advanced Light Source, beamline 12.2.2 (LBNL). The Advanced Light Source was supported by the Director, Office of Science, Office of Basic Energy Sciences, of the U.S. Department of Energy under Contract no. DE-AC02-05CH11231. Partial support for the operation of ALS beamline 12.2.2 was provided by COMPRES, the Consortium for Materials Properties Research in Earth Sciences under NSF Cooperative Agreement EAR1606856.

Conflict of Interest

The authors declare no conflict of interest.

Keywords

diamond anvil cell, radial X-ray diffraction, superhard, transition metal borides

Received: January 10, 2019
Revised: February 11, 2019
Published online: April 3, 2019

[1] M. T. Yeung, R. Mohammadi, R. B. Kaner, *Annu. Rev. Mater. Res.* **2016**, *46*, 465.
[2] M. L. Cohen, *Science* **1993**, *261*, 307.
[3] I. Aleksandrov, A. Goncharov, A. Zisman, S. Stishov, *Zh. Eksp. Teor. Fiz.* **1987**, *93*, 691.
[4] J. B. Levine, S. H. Tolbert, R. B. Kaner, *Adv. Funct. Mater.* **2009**, *19*, 3519.
[5] R. Komanduri, M. C. Shaw, *Nature* **1975**, *255*, 211.
[6] J. E. Westraadt, I. Sigalas, J. H. Neethling, *Int. J. Refract. Met. Hard Mater.* **2015**, *48*, 286.
[7] R. Mohammadi, A. T. Lech, M. Xie, B. E. Weaver, M. T. Yeung, S. H. Tolbert, R. B. Kaner, *Proc. Natl. Acad. Sci. U. S. A.* **2011**, *108*, 10958.
[8] R. Mohammadi, M. Xie, A. T. Lech, C. L. Turner, A. Kavner, S. H. Tolbert, R. B. Kaner, *J. Am. Chem. Soc.* **2012**, *134*, 20660.
[9] M. Xie, R. Mohammadi, Z. Mao, M. M. Armentrout, A. Kavner, R. B. Kaner, S. H. Tolbert, *Phys. Rev. B* **2012**, *85*, 064118.
[10] A. T. Lech, C. L. Turner, R. Mohammadi, S. H. Tolbert, R. B. Kaner, *Proc. Natl. Acad. Sci. U. S. A.* **2015**, *112*, 3223.
[11] E. Lassner, *Tungsten: Properties, Chemistry, Technology of the Element, Alloys, and Chemical Compounds*, Kluwer Academic/Plenum Publishers, New York **1999**.
[12] G. Akopov, I. Roh, Z. C. Sobell, M. T. Yeung, L. Pangilinan, C. L. Turner, R. B. Kaner, *J. Am. Chem. Soc.* **2017**, *139*, 17120.
[13] G. Akopov, M. T. Yeung, R. B. Kaner, *Adv. Mater.* **2017**, *29*, 1604506.
[14] A. T. Lech, C. L. Turner, R. Mohammadi, S. H. Tolbert, R. B. Kaner, *Proc. Natl. Acad. Sci. U. S. A.* **2015**, *112*, 3223.
[15] M. Xie, R. Mohammadi, C. L. Turner, R. B. Kaner, A. Kavner, S. H. Tolbert, *Phys. Rev. B* **2014**, *90*, 104104.
[16] G. Akopov, M. T. Yeung, I. Roh, Z. C. Sobell, H. Yin, W. H. Mak, S. I. Khan, R. B. Kaner, *Chem. Mater.* **2018**, *30*, 3559.
[17] V. I. Matkovich, J. Economy, R. F. Giese, R. Barrett, *Acta Crystallogr.* **1965**, *19*, 1056.
[18] Y. Liang, Y. Zhang, H. Jiang, L. Wu, W. Zhang, K. Heckenberger, K. Hofmann, A. Reitz, F. C. Stober, B. Albert, *Chem. Mater.* **2019**, *31*, 1075.
[19] A. Kavner, M. B. Weinberger, R. B. Kaner, S. H. Tolbert, *J. Appl. Phys.* **2012**, *112*, 013526.
[20] H.-Y. Chung, M. B. Weinberger, J. B. Levine, A. Kavner, J.-M. Yang, S. H. Tolbert, R. B. Kaner, *Science* **2007**, *316*, 436.
[21] A. T. Lech, C. L. Turner, J. Lei, R. Mohammadi, S. H. Tolbert, R. B. Kaner, *J. Am. Chem. Soc.* **2016**, *138*, 14398.
[22] G. Akopov, M. T. Yeung, Z. C. Sobell, C. L. Turner, C. Lin, R. B. Kaner, *Chem. Mater.* **2016**, *28*, 6605.
[23] G. Akopov, Z. C. Sobell, M. T. Yeung, R. B. Kaner, *Inorg. Chem.* **2016**, *55*, 12419.
[24] G. Akopov, M. T. Yeung, C. L. Turner, R. L. Li, R. B. Kaner, *Inorg. Chem.* **2016**, *55*, 5051.
[25] T. Ma, H. Li, X. Zheng, X. Zheng, S. Wang, X. Wang, H. Zhao, S. Han, J. Liu, R. Zhang, P. Zhu, Y. Long, J. Cheng, Y. Ma, Y. Zhao, C. Jin, Y. Yu, *Adv. Mater.* **2017**, *29*, 1604003.
[26] S. La Placa, I. Binder, B. Post, *J. Inorg. Nucl. Chem.* **1961**, *18*, 113.
[27] J. C. Slater, *J. Chem. Phys.* **1964**, *41*, 3199.
[28] R. J. Hemley, H. K. Mao, G. Shen, J. Badro, P. Gillet, M. Hanfland, D. Häusermann, *Science* **1997**, *276*, 1242.
[29] E. H. Yoffe, *Philos. Mag. A* **1982**, *46*, 617.
[30] N. Korozlu, K. Colakoglu, E. Deligoz, S. Aydin, *J. Alloys Compd.* **2013**, *546*, 157.
[31] Y. Lv, X. Zhang, W. Jiang, *Ceram. Int.* **2018**, *44*, 128.
[32] H. K. Mao, J. F. Shu, G. Y. Shen, R. J. Hemley, B. S. Li, A. K. Singh, *Nature* **1998**, *396*, 741.
[33] S. Merkel, *J. Phys.: Condens. Matter* **2006**, *18*, S949.
[34] T. S. Duffy, *AIP Conf. Proc.* **2007**, *955*, 639.
[35] R. J. Hemley, H. K. Mao, G. Shen, J. Badro, P. Gillet, M. Hanfland, D. Hausermann, *Science* **1997**, *276*, 1242.
[36] D. He, T. S. Duffy, *Phys. Rev. B* **2006**, *73*, 134106.
[37] T. S. Duffy, G. Shen, D. L. Heinz, J. Shu, Y. Ma, H. K. Mao, R. J. Hemley, A. K. Singh, *Phys. Rev. B* **1999**, *60*, 15063.
[38] S. R. Shieh, T. S. Duffy, B. S. Li, *Phys. Rev. Lett.* **2002**, *89*, 255507.
[39] A. Kavner, T. S. Duffy, *Phys. Rev. B* **2003**, *68*, 144101.
[40] D. He, S. R. Shieh, T. S. Duffy, *Phys. Rev. B* **2004**, *70*, 184121.
[41] M. T. Yeung, J. Lei, R. Mohammadi, Y. Wang, S. H. Tolbert, R. B. Kaner, *Adv. Mater.* **2016**, *28*, 6993.
[42] J. Lei, M. T. Yeung, P. J. Robinson, R. Mohammadi, C. L. Turner, J. Yan, A. Kavner, A. N. Alexandrova, R. B. Kaner, S. H. Tolbert, *J. Phys. Chem. C* **2018**, *122*, 5647.
[43] D. D. Ragan, D. R. Clarke, D. Schiferl, *Rev. Sci. Instrum.* **1996**, *67*, 494.
[44] Y. R. Shen, R. S. Kumar, M. Pravica, M. F. Nicol, *Rev. Sci. Instrum.* **2004**, *75*, 4450.
[45] A. Dewaele, P. Loubeyre, *High Pressure Res.* **2007**, *27*, 419.
[46] L. Dubronvinsky, N. Dubrovinskaia, E. Bykova, M. Bykov, V. Prakapenka, C. Prescher, K. Glazyrin, H. Liermann, M. Hanfland, M. Ekholm, Q. Feng, L. Pourovskii, M. Katsnelson, J. Wills, A. Abrikosov, *Nature* **2015**, *525*, 226.
[47] L. Vegard, *Eur. Phys. J. A* **1921**, *5*, 17.
[48] C. Meade, R. Jeanloz, *Geophys. Res. Lett.* **1990**, *17*, 1157.
[49] R. B. Kaner, J. J. Gilman, S. H. Tolbert, *Science* **2005**, *308*, 1268.
[50] A. E. Baranovsky, G. E. Grechnev, V. D. Fil, T. V. Ignatova, A. V. Logosha, A. S. Panfilov, I. V. Svechkarev, N. Y. Shitsevalova, V. B. Filippov, O. Eriksson, *J. Alloys Compd.* **2007**, *442*, 228.
[51] G. E. Grechnev, A. E. Baranovskiy, V. D. Fil, T. V. Ignatova, I. G. Kobolov, A. V. Logosha, *Low Temp. Phys.* **2008**, *34*, 921.
[52] J. Schiøtz, F. D. Di Tolla, K. W. Jacobsen, *Nature* **1998**, *391*, 561.
[53] J. Schiøtz, K. W. Jacobsen, *Science* **2003**, *301*, 1357.
[54] B. Chen, K. Lutker, S. V. Raju, J. Yan, W. Kanitpanyacharoen, J. Lei, S. Yang, H.-R. Wenk, H.-K. Mao, Q. Williams, *Science* **2012**, *338*, 1448.
[55] B. Chen, K. Lutker, J. Lei, J. Yan, S. Yang, H. Mao, *Proc. Natl. Acad. Sci. U. S. A.* **2014**, *111*, 3350.
[56] X. Zhou, N. Tamura, Z. Mi, J. Lei, J. Yan, L. Zhang, W. Deng, F. Ke, B. Yue, B. Chen, *Phys. Rev. Lett.* **2017**, *118*, 096101.
[57] M. B. Kanoun, P. Hermet, S. Goumri-Said, *J. Phys. Chem. C* **2012**, *116*, 11746.
[58] D. G. Isaak, *Handbook of Elastic Properties of Solids, Liquids, and Gases*, Academic Press, San Diego, CA **2001**.
[59] H. Dong, S. M. Dorfman, Y. Chen, H. Wang, J. Wang, J. Qin, D. He, T. S. Duffy, *J. Appl. Phys.* **2012**, *111*, 123514.
[60] G. Akopov, M. T. Yeung, C. L. Turner, R. Mohammadi, R. B. Kaner, *J. Am. Chem. Soc.* **2016**, *138*, 5714.
[61] M. Xie, R. Mohammadi, C. L. Turner, R. B. Kaner, A. Kavner, S. H. Tolbert, *Appl. Phys. Lett.* **2015**, *107*, 041903.
[62] J. Lei, M. T. Yeung, R. Mohammadi, C. L. Turner, J. Yan, R. B. Kaner, S. H. Tolbert, *J. Appl. Phys.* **2019**, *125*, 082529.
[63] S. Merkel, T. Yagi, *Rev. Sci. Instrum.* **2005**, *76*, 046109.
[64] S. Merkel, H. R. Wenk, J. Shu, G. Shen, P. Gillet, H. K. Mao, R. J. Hemley, *J. Geophys. Res.: Solid Earth* **2002**, *107*, ECV 3.
[65] A. P. Hammersley, S. O. Svensson, M. Hanfland, A. N. Fitch, D. Hausermann, *High Pressure Res.* **1996**, *14*, 235.
[66] A. K. Singh, H.-K. Mao, J. Shu, R. J. Hemley, *Phys. Rev. Lett.* **1998**, *80*, 2157.
[67] A. K. Singh, *J. Appl. Phys.* **1993**, *73*, 4278.
[68] A. K. Singh, C. Balasingh, H.-K. Mao, R. J. Hemley, J. Shu, *J. Appl. Phys.* **1998**, *83*, 7567.
[69] A. L. Ruoff, *J. Appl. Phys.* **1975**, *46*, 1389.
[70] A. K. Singh, *J. Appl. Phys.* **2009**, *106*, 043514.
[71] W. Voigt, *Lehrbuch der Kristallphysik*, Teubner, Leipzig **1928**.
[72] A. Reuss, *Z. Angew. Math. Mech.* **1929**, *9*, 49.
[73] R. F. S. Hearmon, *Adv. Phys.* **1956**, *5*, 323.
[74] G. M. Amulele, M. H. Manghnani, M. Somayazulu, *J. Appl. Phys.* **2006**, *99*, 023522.
[75] D. W. He, S. R. Shieh, T. S. Duffy, *Phys. Rev. B* **2004**, *70*, 184121.
[76] F. Birch, *J. Geophys. Res.* **1978**, *83*, 1257.